Journal of Solid State Chemistry **150,** 145–153 (2000)
doi:10.1006/jssc.1999.8570, available online at http://www.idealibrary.com on IDEAL®

Relationships between Structure and Physical Properties in $SmNi_{1-x}Co_xO_3$

J. Pérez-Cacho,* J. Blasco,*,[1] J. García,* and R. Sanchez†

*Instituto de Ciencia de Materiales de Aragón y Departamento de Física de la Materia Condensada, Consejo Superior de Investigaciones Científicas—Universidad de Zaragoza, Pedro Cerbuna 12, 50009 Zaragoza, Spain; and †Centro atómico de Bariloche, 8400 San Carlos de Bariloche (RN), Argentina

Received May 11, 1999; in revised form October 8, 1999; accepted November 5, 1999

The crystal structure of $SmNi_{1-x}Co_xO_3$ perovskites, with $0 \leq x \leq 1$, has been determined at room temperature by Rietveld analysis from X-ray powder diffraction data. Polycrystalline samples have been prepared using high temperature and high oxygen pressure treatment. Different structural parameters such as the bond lengths or the bond angles, have been compared to the Ni/Co ratio. They have also been correlated with the magnetic and electrical properties of the series. $SmNi_{1-x}Co_xO_3$ are orthorhombic perovskites, space group *Pbnm*. The expected linear dependence in the oxygen-transition metal bondlengths, d_{M-O}, for a solid solution, which is often described by the Vergard's law, is modulated by slight structural changes. In the $0.3 \leq x < 0.9$ range, an anomalous increase in d_{M-O} can be correlated to the ferromagnetic interactions shown by these samples at low temperatures. In addition, in the $x \leq 0.1$ range, there is a decrease in the orthorhombic distortion of the crystal structure along the series which agrees with a composition-driven metal insulator transition at room temperature. These structural features point out the phase diagram proposed earlier for the $SmNi_{1-x}Co_xO_3$ series. © 2000 Academic Press

Key Words: **perovskite; metal–insulator transition; spin-glass; Rietveld analysis; bond valence calculation.**

1. INTRODUCTION

The study of transition metal oxides with perovskite structure is of great interest nowadays. The rich variety of physical properties such as high-temperature superconductivity, giant magnetoresistance, or metal–insulator transitions makes this study very attractive for both academic and technological purposes (1). Most of these compounds show a relationship between small structural changes and their physical properties (2). Crystal structure variations are often labeled as either the cause or the effect of a macroscopic transformation. The understanding of these macroscopic properties needs an accurate structural determination. $SmNiO_3$, $SmCoO_3$, and $SmNi_{1-x}Co_xO_3$ belong to this family of oxides and show interesting features not yet well understood (3).

$SmNiO_3$ shows a temperature-driven metal–insulator (MI) transition at 400 K and develops an antiferromagnetic (AF) ordering at 220 K (4). The electronic localization has been discussed in terms of either strong electronic correlation or AF polaronic effects (5). $RNiO_3$ (R = La, Pr, Nd, Sm, Eu) shows a complex phase diagram, which consists of paramagnetic metal, paramagnetic insulator, and AF insulator regions whose boundaries change with the rate earth size (4). Several kinds of orbital ordering have been proposed to explain the complex low temperature AF arrangement (6). Recently, Alonso *et al.* (7) have found structural changes at the MI transition in $YNiO_3$. This result seems to indicate a charge disproportion in the Ni sublattice in the insulating phase. In summary, $RNiO_3$ series provide a remarkable opportunity to compare structural features (the superexchange Ni–O–Ni angle or the strain of the Ni–O distance) with the evolution of several transport and magnetic macroscopic properties (8).

On the other hand, $RCoO_3$ (R = rare earth) oxides display examples of temperature-dependent electronic and spin-state transitions. The ground state of $LaCoO_3$ is a nonmagnetic insulator whose Co^{3+} configuration is of low spin (LS), $t_{2g}^6 e_g^0$ ($\mathbf{S} = 0$). The relative energy ratio between the octahedral Co^{3+} crystal-field splitting and the intraatomic Hund coupling can change with temperature, leading to different transitions from LS to either thermally excited high spin (HS), $t_{2g}^4 e_g^2$ ($\mathbf{S} = 2$), or intermediate spin (IS), $t_{2g}^5 e_g^1$ ($\mathbf{S} = 1$), configuration (9). These variations in the electronic states are then straightly monitored by the magnetic susceptibility. However, the variation of cobalt configuration with temperature is still under discussion (10). In addition, $RCoO_3$ oxides show a crossover from a semiconducting to a metallic regime above 500 K. The MI transition

[1]To whom correspondence should be addressed. E-mail: jbc@posta.unizar.es.

0022-4596/00 $35.00

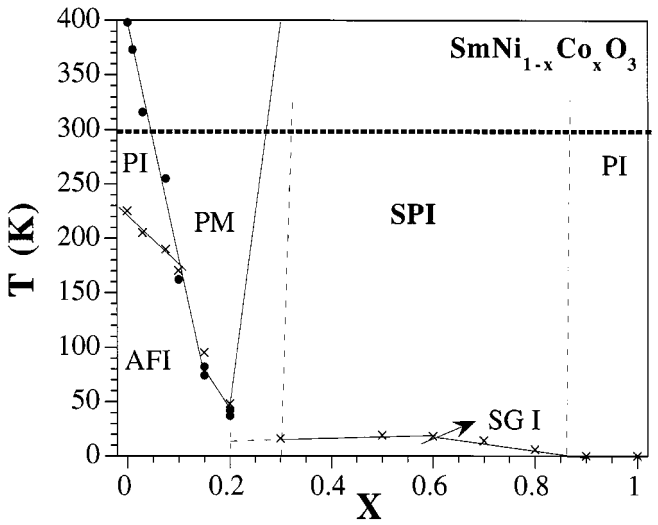

FIG. 1. Schematic phase diagram of the $SmNi_{1-x}Co_xO_3$ series. Cobalt concentration (x) is shown along the x axis and temperature along y axis. Solid circles correspond to T_{MI} temperatures, crosses correspond to either Néel temperatures or spin freezing temperatures, and open circles correspond to the MI transition. AF represents antiferromagnetic regime, SG spin-glass-like, P paramagnetism, M metallic, and I the two semiconducting regimes in the series. **SPI** refers to the paramagnetic region where paramagnetic effective moments are higher than the expected moments for Ni^{3+} and Co^{3+} in low-spin state. Solid lines are the proposed boundary regions. The broken bold line indicates the region covered b X-ray diffraction measurements.

temperature (T_{MI}) varies in $RCoO_3$ series with the Co–O–Co superexchange angle, for $SmCoO_3$ T_{MI} is 600 K (11).

Recently, we have studied the physical properties of the $SmNi_{1-x}Co_xO_3$ series. Figure 1 shows a detail of the proposed phase diagram (3). These oxides, depending on the Ni/Co ratio, display both AF and ferromagnetic interactions and both metallic and semiconducting conduction. Below $x \leq 0.2$, both the electronic localization and the AF ordering temperatures observed in $SmNiO_3$ decrease with increasing x, inducing a paramagnetic metallic regime at room temperature, i.e., a MI transition driven by cobalt doping. Between $x = 0.2$ and 0.3, a new semiconducting regime appears and short range ferromagnetic interactions are evident at lower temperatures. For $0.3 \leq x < 0.9$, the competition between ferro and AF interactions gives rise to a semiconducting spin-glass-like regime. One of the most interesting result in this series is the determination of large magnetoresistance effects in the spin-glass-like region (12). This feature is also shown by other members of the $RNi_{1-x}Co_xO_3$ series, where Sm is replaced by other rare earth ions (13).

The aim of the present work is to determine with accuracy the crystal structure of $SmNi_{1-x}Co_xO_3$ in order to correlate structural parameters and macroscopic properties. We are especially interested in the electronic configurations of transition metal ions and possible interactions among them. $SmNi_{1-x}Co_xO_3$ series has been prepared and characterized by X-ray powder diffraction, thermogravimetric analysis, and magnetic measurements. We have performed Rietveld refinements in the whole series and the obtained bond lengths, bond angles, and the bond-strain have been compared to the current conduction properties and to the magnetic properties.

2. EXPERIMENTAL

$SmNi_{1-x}Co_xO_3$ samples ($x = 0$, 0.03, 0.075, 0.1, 0.15, 0.2, 0.3, 0.5, 0.7, and 0.9) were prepared under high oxygen pressure from a precursor obtained by means of a citrate sol–gel route. A stoichiometric mixture of Sm_2O_3, Co, and $2NiCO_3 3Ni(OH)_2 4H_2O$ was first dissolved in a nitric acid solution, and then appropriate amounts of citric acid and ethylene glycol were added. Such solutions were heated until green–red gels were formed. These gels were dried by heating at 300°C. In order to obtain the precursors, the remaining brown powders were calcined in alumina crucibles overnight with flow of oxygen at 500°C. These precursors were pressed to 5 Kbar and sintered in a Morris Research furnace at 1000°C and at 200 bar of oxygen pressure for 12 h. $SmCoO_3$ was prepared by standard solid state ceramic procedures at 1200°C in air, with some intermediate grindings.

Step-scanned X-ray diffraction (XRD) patterns were collected at room temperature using a D-max Rigaku system with a rotating anode. A graphite monochromator selected the $CuK\alpha_{1,2}$ radiation. Data were collected from 18° up to 140° in 2θ with a step size of 0.02° and a counting time of 8 s per step. All XRD data were analyzed by the Rietveld method using the Fullprof program (14). Bond valence analysis (15) have been performed by using the Valist calculation program (16). Bond valence analysis has been used for both quantitative measurement of the bond strain and possible assignment of the oxidation state.

The oxygen content for $SmNi_{1-x}Co_xO_{3-\delta}$ samples was determined from thermogravimetric analysis. A Texas Instrument TGA system was used in a reducing N_2/H_2 (95:5) flow, working at a heating rate of 10°C/min. A small oxygen deficiency was detected in $SmNiO_{3-\delta}$ ($\delta = 0.04$), while all other $SmNi_{1-x}Co_xO_{3-\delta}$ oxides show a nearly perfect stoichiometric composition, with $\delta = 0.00 \pm 0.02$. dc magnetization measurements were carried out between 5 and 700 K. A commercial Quantum Design (SQUID) magnetometer was used in the measurements up to 350 K. Experiments in the $350 \leq T \leq 700$ K temperature range were performed in a vibrating sample magnetometer.

3. RESULTS AND DISCUSSION

The analysis of the X-ray diffraction patterns indicates single-phase compounds for all $SmNi_{1-x}Co_xO_3$, $0 \leq x \leq 1$,

samples at room temperature. Observed Bragg peaks can be indexed in the orthorhombic *Pbnm* space group (standard setting *Pnma*, no. 62). This is one of the most common distorted structures derived from the cubic perovskite. The origin for this orthorhombic distortion is the free space left in the cubic perovskite lattice ($a_p \approx 4$ Å), due to the small rare-earth size. The cubic structure has then relaxed to a lower space group symmetry through slight tilts of the transition metal–oxygen octahedra, MO_6, around the pseudocubic axes. The *Pbnm* space group appears when MO_6 tilts are of $a^-a^-c^+$ type in Glazer's terminology (17). $a \approx \sqrt{2}a_p$, $b \approx \sqrt{2}a_p$, and $c \approx 2a_p$ are the new orthorhombic unit-cell parameters, where a and b axes are found in the $\{1\,1\,0\}$ diagonal of the pseudocubic lattice and the c axis has doubled its cubic value. This structure can also be understood as a tilt of $a^0b^+c^+$ type around the new orthorhombic axes. Figure 2 shows this distorted perovskite lattice.

In the *Pbnm* RMO_3 perovskite, rare-earth cations (R) are placed in 4c sites $\pm(x, y, \frac{1}{4}; \frac{1}{2}-x, \frac{1}{2}+y, \frac{1}{4})$, the transition metal cations (M) in 4b sites on the symmetry center $(\frac{1}{2}, 0, 0; \frac{1}{2}, 0, \frac{1}{2}; 0, \frac{1}{2}, 0; 0\,\frac{1}{2}, \frac{1}{2})$. Oxygen ions are in two different atomic positions, the equatorial oxygens, O(II), are in 8d $\pm(x, y, z; \frac{1}{2}-x, \frac{1}{2}+y, \frac{1}{2}-z; -x, -y, \frac{1}{2}+z; \frac{1}{2}+x, \frac{1}{2}-y, -z)$ and the apical oxygens, O(I), are in 4c sites. There is only one available site for the M atoms in this structure. Therefore, the absence of any superstructure diffraction peak points to a random substitution of Co and Ni ions. Lattice parameters, fractional atomic coordinates and isotropic temperture factors were obtained from the Rietveld analysis. A pseudo-Voigt function was selected as the diffraction peak shape function. Background coefficients, zero point, a scale factor, an asymmetry parameter for the shape of the peak and profile shape parameters were also refined in the final run. As an example, Fig. 3 displays the observed and calculated diffraction pattern for $SmNi_{0.3}Co_{0.7}O_3$. The refined structural parameters are listed in Tables 1 and 2 for all the samples. Figure 4 shows the evolution of the lattice parameters and the unit cell volume along the series.

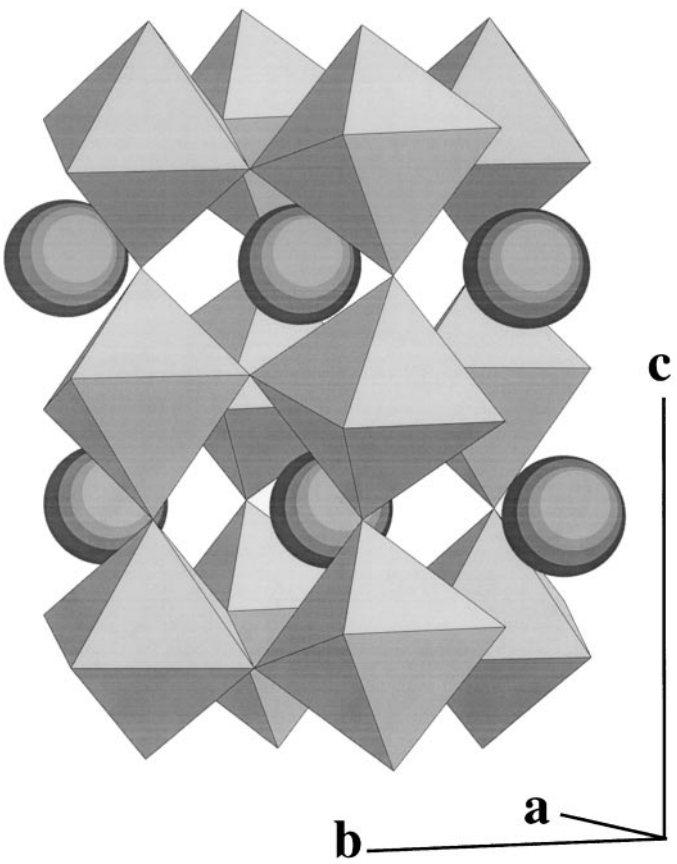

FIG. 2. View of the *Pbnm* perovskite structure for $SmNiO_3$. Ballshapes correspond to Sm^{3+} ions. Oxide and Ni^{3+} ions are located at the corner and in the center of the octahedra, respectively.

On the other hand, bond valence calculations were performed. Bond valence model (15) describes a phenomenological correlation between the formal valence of a bond and the bondlengths around it. Here, the valence of a bond is a quantity whose sum around each atom, i, must be equal to its oxidation state, V_i; $V_i = \sum_j S_{ij}$, being S_{ij} the valence of a bond between two atoms i and j. This model assumes that both cation and anion coordination spheres should be as regular as possible (15). Therefore, there is a set of ideal bond lengths and any deviation from these ideal lengths can be ascribed either to electronic effects or to steric effects. In the $SmNi_{1-x}Co_xO_3$ series, both kind of effects are expected. On the one hand, the crystal structure is distorted due to the small size of Sm^{3+}. On the other hand, a high degree of covalency is expected for these compounds due to the mixing of metal 3d orbitals and oxygen 2p orbitals (18). Refined bondlengths for $SmNi_{1-x}Co_xO_3$ compounds were introduced in the VaList program (16) in order to have an indication of the correct oxidation state of the M. M^{2+}, M^{3+}, and M^{4+} configurations for nickel and cobalt ions were checked, and Table 3 lists these calculations for a selected number of samples. LS Ni^{3+} and LS Co^{3+} are the most self-consistent configurations with the refined crystallographic parameters. A similar bond-strain is observed for each d_{M-O} in the whole series considering these configurations. Bond valence calculations for d_{M-O} must be carefully analyzed; d_{M-O} are only crystallographic averages of both, the d_{Ni-O} and the d_{Co-O} distances and the results must be only considered as a rough approximation of the electronic state for the M atoms. The results of Table 3 seem to indicate that LS Ni^{3+} is underbonded in $SmNiO_3$ and it is becoming normal bonded in the $SmNi_{1-x}Co_xO_3$ samples with increasing Co content. However, the opposite is correct for LS Co^{3+}, it is normal bonded in the end member, $SmCoO_3$, but underbonded in $SmNi_{1-x}Co_xO_3$ samples.

The structural parameters obtained in the Rietveld analysis for the end members of the series, $SmNiO_3$ and

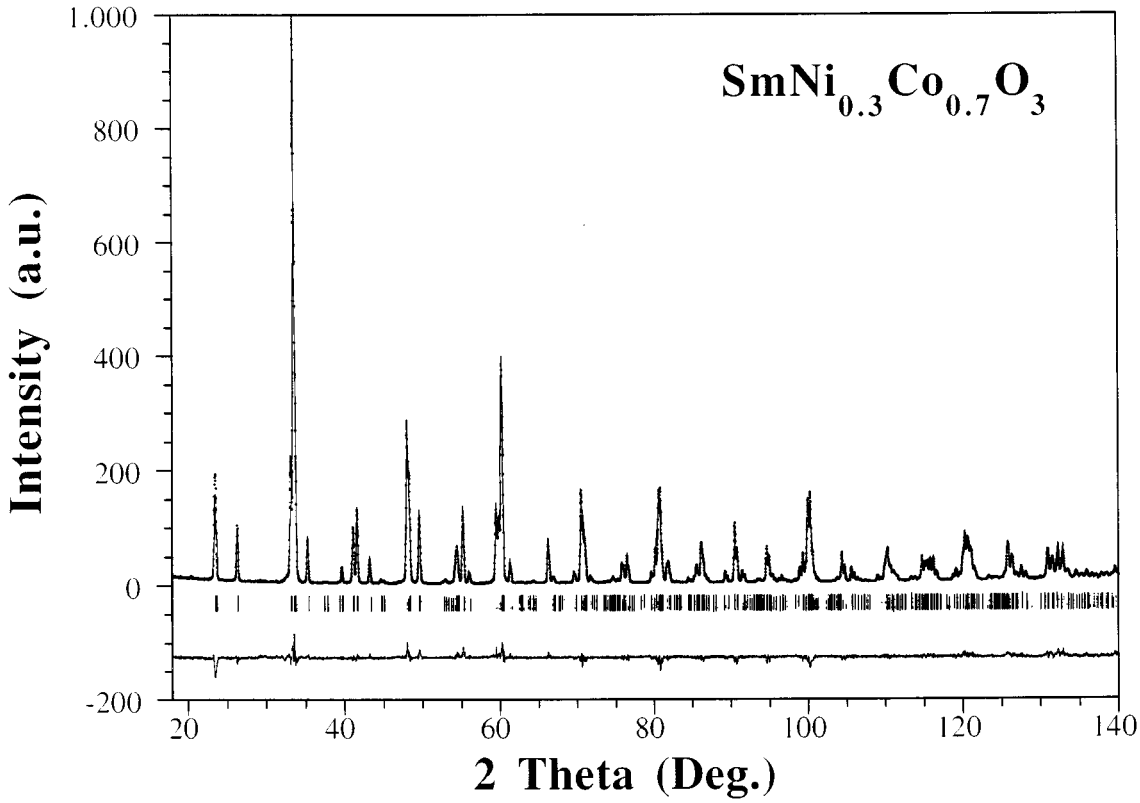

FIG. 3. Rietveld refinement plot (line) of the X-ray powder diffraction data for $SmNi_{0.3}Co_{0.7}O_3$ at room temperature (points). The bars indicate the allowed Bragg reflections. The difference curve between observed and calculated profiles is plotted at the bottom.

$SmCoO_3$, agree with the earlier reported values (19, 20). In these previous studies, $SmNiO_3$ and $SmCoO_3$ perovskites were compared with others $RNiO_3$ and $RCoO_3$ oxides (R = rare earth). In the RMO_3 series, when the size of the R^{3+} ions decreases from La^{3+} to Lu^{3+} (lanthanide contraction), the distortion increases, dealing to a well known structural effect. MO_6 octahedron increase their rotation around the pseudocubic axes in order to optimize d_{M-O}, and the angle between adjacent MO_6 octahedra, the so-called $\langle M\text{–}O\text{–}M\rangle$ superexchange angle, goes farther from the theoretically 180° value of the cubic perovskite (19–21). However, in $SmNi_{1-x}Co_xO_3$, as the tilt of the octahedra does not change practically ($\langle M\text{–}O\text{–}M\rangle \approx 153.5°$) structural variations in the series are much smaller. The variations in $SmNi_{1-x}Co_xO_3$ should then mainly have been a result of the steric differences of the M ionic sizes, most of all between LS Co^{3+} and LS Ni^{3+} configurations. $SmCoO_3$ unit cell is 6.38 $Å^3$ smaller than $SmNiO_3$. This difference agrees quite well with the difference in ionic size between low spin Ni^{3+} and low spin Co^{3+}, 0.56 and 0.545 Å, respectively (22, 23).

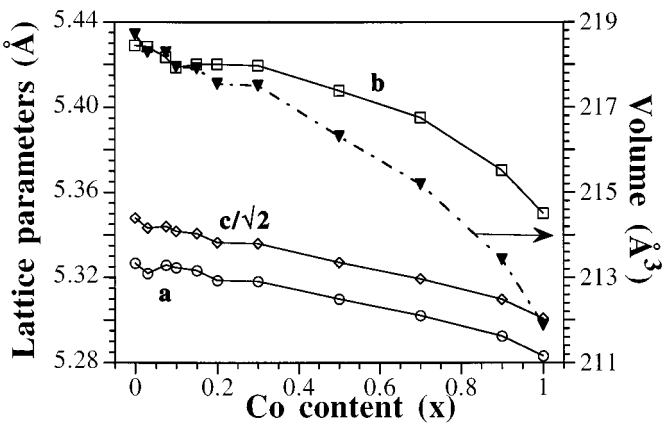

FIG. 4. Volume and lattice parameters vs cobalt concentration for the $SmNi_{1-x}Co_xO_3$ series.

Homogenous and random solid solutions usually obey the so-called Vegard's law, i.e., a linear dependence between composition and structural parameters (24). In $SmNi_{1-x}Co_xO_3$, over the linear dependence of the structural parameters, see Fig. 4, there are some nonlinear modulations. They likely suggest that the structure variations are not only due to steric effects, and some electronic factors must also be considered in the M sublattice. This is an expected result if we look at the phase diagram proposed in

TABLE 1
Refined Lattice Parameters, Unit Cell Volume, Fractional Atomic Coordinates, Isotropic Temperature Factors, and Reliability (Unweighted, Weighted, Expected, and Bragg) Factors (%) as Defined in Ref. (14)

	$SmNiO_3$	$x = 0.03$	$x = 0.075$	$x = 0.1$	$x = 0.15$	$x = 0.2$	$x = 0.3$	$x = 0.5$	$x = 0.7$	$x = 0.9$	$x = 1$
a (Å)	5.3268(1)	5.3219(1)	5.3259(2)	5.3246(1)	5.3232(1)	5.3185(1)	5.3182(1)	5.3099(1)	5.3021(1)	5.2925(1)	5.2831(1)
b (Å)	5.4289(1)	5.4283(1)	5.4234(2)	5.4185(1)	5.4201(1)	5.4200(1)	5.4195(1)	5.4078(1)	5.3952(1)	5.3704(1)	5.3502(1)
c (Å)	7.5630(2)	7.5564(2)	7.5576(3)	7.5544(2)	7.5528(2)	7.5469(2)	7.5462(2)	7.5335(2)	7.5226(1)	7.5090(1)	7.4962(1)
Vol. (Å^3)	218.71	218.30	218.29	217.95	217.91	217.55	217.50	216.32	215.19	213.43	211.88
Sm: x	0.9898(2)	0.9903(2)	0.9902(2)	0.9904(2)	0.9903(2)	0.9900(2)	0.9905(2)	0.9900(2)	0.9904(1)	0.9906(1)	0.9908(2)
y	0.510(1)	0.0510(1)	0.0503(1)	0.0497(1)	0.0499(1)	0.0503(1)	0.0507(1)	0.0501(1)	0.0493(1)	0.0480(1)	0.0467(1)
B (Å^2)	0.22(1)	0.27(1)	0.35(2)	0.17(2)	0.35(1)	0.04(1)	0.05(2)	0.23(2)	0.58(1)	0.03(1)	0.26(1)
M: B (Å^2)	0.26(3)	0.37(3)	0.45(4)	0.33(3)	0.47(3)	0.16(3)	0.33(6)	0.05(3)	0.85(3)	0.30(2)	0.43(2)
O(I): x	0.082(1)	0.079(1)	0.082(1)	0.083(1)	0.084(1)	0.083(1)	0.085(1)	0.083(1)	0.082(1)	0.084(1)	0.083(1)
y	0.485(1)	0.487(1)	0.482(1)	0.483(1)	0.482(1)	0.484(1)	0.487(1)	0.486(1)	0.486(1)	0.489(1)	0.488(1)
B (Å^2)	0.47(10)	1.08(9)	0.71(17)	0.24(12)	0.81(10)	0.06(10)	1.23(19)	0.29(12)	0.80(9)	0.30(9)	0.14(14)
O(II): x	0.707(1)	0.707(1)	0.709(1)	0.709(1)	0.710(1)	0.710(1)	0.708(1)	0.706(1)	0.707(1)	0.703(1)	0.708(1)
y	0.296(1)	0.294(1)	0.291(1)	0.290(1)	0.291(1)	0.291(1)	0.292(1)	0.291(1)	0.292(1)	0.293(1)	0.289(1)
z	0.0439(8)	0.0448(8)	0.043(1)	0.0437(8)	0.0425(9)	0.0435(8)	0.0420(8)	0.0416(8)	0.0410(8)	0.0393(7)	0.0392(9)
B (Å^2)	0.05(5)	0.88(6)	0.42(9)	0.42(6)	0.68(7)	0.36(6)	1.09(16)	0.20(7)	0.98(5)	0.33(5)	0.57(7)
R_p/R_{wp}	10.1/12.7	7.2/9.4	8.6/11.7	7.0/9.0	6.9/8.9	6.8/8.8	7.8/10.3	7.4/9.6	7.2/9.6	7.1/9.4	7.9/10.5
R_{exp}	4.6	4.4	4.7	5.2	4.3	3.8	4.1	4.4	6.0	4.4	5.2
R_{Bragg}	6.1	5.4	6.1	5.1	5.4	5.4	4.5	5.6	5.1	4.9	5.6

Note. M = Ni/Co. Standard deviations are shown in parentheses.

Fig. 1. At room temperature, depending on the x value, different electronic and magnetic regimes are described. Samples with $x \leq 0.03$ are semiconducting, and the conductivity increases with increasing x value and ranges from 4 to 40 S cm^{-1}. For $0.075 \leq x \leq 0.2$, the samples are metallic and conductivity takes values of around 300 S cm^{-1}. Finally, the samples become again semiconducting for $x \geq 0.3$ and the conductivity decreases with increasing Co content ranging from 225 to 3 S cm^{-1}. Magnetic behavior also changes along the series with x. Though all the samples are paramagnetic at room temperature, ferromagnetic interactions are evident for samples with $0.3 \leq x < 0.9$ at low temperatures (3). Their ground states are spin-glass like with a cusp temperature ranging between 8 and 20 K. These features have been explained on the basis of high Ni^{3+} electronegativity that can induce either a charge transfer between Ni^{3+} and Co^{3+} or the stabilization of different Co^{3+} configurations such as HS or IS (3). Consequently, the samples show higher effective paramagnetic moments than the expected moments for LS Ni^{3+} and LS Co^{3+} configura-

TABLE 2
Interatomic Distances (Å) and Angles (Deg.) for M–O Octahedron and Interatomic Distances (Å) for Sm–O Dodecahedron

	No.	$SmNiO_3$	$x = 0.03$	$x = 0.075$	$x = 0.1$	$x = 0.15$	$x = 0.2$	$x = 0.3$	$x = 0.5$	$x = 0.7$	$x = 0.9$	$x = 1$
M–O(I)	2	1.942(2)	1.936(2)	1.941(2)	1.942(2)	1.943(2)	1.940(2)	1.942(2)	1.936(2)	1.932(2)	1.930(2)	1.926(2)
M–O(II)	2	1.977(5)	1.971(5)	1.959(8)	1.955(6)	1.959(7)	1.961(6)	1.957(6)	1.953(6)	1.943(5)	1.930(5)	1.920(6)
	2	1.941(5)	1.946(5)	1.947(8)	1.948(6)	1.942(7)	1.941(6)	1.945(6)	1.942(6)	1.943(5)	1.946(5)	1.933(6)
$\langle M$–O$\rangle$		1.954	1.951	1.949	1.948	1.948	1.947	1.948	1.943	1.939	1.935	1.926
M–O(I)–M	2	153.5(1)	154.7(1)	153.4(1)	153.0(1)	152.8(1)	153.0(1)	152.5(1)	153.3(1)	153.4(1)	153.1(1)	153.4(1)
M–O(II)–M	4	152.1(2)	152.0(2)	153.3(3)	153.4(3)	153.7(3)	153.3(3)	153.2(3)	153.3(2)	153.4(2)	153.1(2)	154.6(3)
$\langle M$–O–$M\rangle$		152.6	152.9	153.3	153.3	153.4	153.2	153.0	153.3	153.4	153.1	154.2
Sm–O(I)	1	3.111(6)	3.097(6)	2.395(9)	3.108(7)	3.118(8)	3.107(7)	3.095(7)	3.087(7)	3.080(7)	3.041(6)	3.027(7)
Sm–O(I)	1	2.407(6)	2.413(6)	3.117(9)	2.401(7)	2.394(8)	2.405(7)	2.419(7)	2.411(7)	2.405(7)	2.421(6)	2.412(7)
Sm–O(I)	1	3.068(7)	3.048(7)	3.068(9)	3.076(9)	3.078(9)	3.071(8)	3.084(9)	3.062(9)	3.057(8)	3.058(8)	3.049(9)
Sm–O(I)	1	2.307(7)	2.320(7)	2.309(9)	2.298(9)	2.297(9)	2.296(8)	2.280(9)	2.293(9)	2.290(8)	2.273(8)	2.272(9)
Sm–O(II)	2	2.540(6)	2.534(6)	2.527(8)	2.521(6)	2.527(7)	2.520(6)	2.538(6)	2.537(6)	2.539(6)	2.560(5)	2.532(6)
Sm–O(II)	2	2.336(6)	2.334(6)	2.355(8)	2.354(6)	2.359(7)	2.352(6)	2.353(6)	2.348(6)	2.344(6)	2.329(6)	2.345(6)
Sm–O(II)	2	2.642(6)	2.645(6)	2.648(8)	2.654(6)	2.645(7)	2.648(6)	2.629(6)	2.623(6)	2.615(6)	2.590(5)	2.606(7)
Sm–O(II)	2	3.329(6)	3.327(6)	3.302(8)	3.296(6)	3.292(7)	3.299(6)	3.300(6)	3.291(6)	3.280(6)	3.273(5)	3.234(7)

Note. M = Ni/Co. Standard deviations are shown in parentheses.

TABLE 3
Valence Sums for the Central Coordinated Atom of the MO_6 Octahedra (M = Co, Ni) in the Perovskite Structure for $SmNi_{1-x}Co_xO_3$ Samples

	$SmNiO_3$	% Dev	$x = 0.1$	% Dev	$x = 0.3$	% Dev	$x = 0.5$	% Dev	$x = 0.7$	% Dev	$x = 1$	% Dev
Ni^{2+}	2.604	30%	2.782	39%	2.786	39%	2.826	41%	2.854	43%	—	—
Ni^{3+}	**2.894**	4%	**2.930**	2%	**2.934**	2%	**2.974**	1%	**3.004**	0%	—	—
Ni^{4+}	3.112	22%	3.152	21%	3.154	21%	3.200	20%	3.232	19%	—	—
LS Co^{2+}	—		2.498	25%	2.500	25%	2.536	27%	2.560	28%	2.650	32%
LS Co^{3+}	—		**2.820**	6%	**2.822**	6%	**2.862**	5%	**2.892**	4%	**2.992**	0%
Co^{4+}	—		3.606	10%	3.610	10%	3.662	8%	3.698	8%	3.828	4%
HS Co^{2+}	—		3.228	61%	3.232	62%	3.280	64%	3.310	66%	3.428	7%
HS Co^{3+}	—		3.362	12%	3.364	12%	3.416	14%	3.448	15%	3.5678	19%

Note. Bond valence sums were performed for different oxidation states. Ni and Co ions can exist in multiple configurations. The most self consistent calculations are displayed in bold. Bond valence sums are based on the empirical relationship $V_i = \sum_j S_{ij} = \sum_{ij} \exp[(R_{ij} - d_{ij})/B]$, where V_i is the oxidation state of the atom, S_{ij} is the valence of a particular bond, R_{ij} is a characteristic parameter of each cation–anion pair, $B = 0.37$ is a universal constant, and d_{ij} is the length of a bond. R_{ij} constants were calculated from the equation $R_{ij} = B \ln[V_i/\sum_j \exp(-d_{ij}/B)]$ (15), and d_{ij} were taken from Refs. (20–21). $R_{Ni^{2+}-O^{2-}} = 1.664$, $R_{Ni^{3+}-O^{2-}} = 1.683$, $R_{Ni^{4+}-O^{2-}} = 1.710$, $R_{Co^{2+}(LS)-O^{2-}} = 1.624$, $R_{Co^{3+}(LS)-O^{2-}} = 1.669$, $R_{Co^{4+}-O^{2-}} = 1.760$, $R_{Co^{2+}(HS)-O^{2-}} = 1.719$, $R_{Co^{3+}(HS)-O^{2-}} = 1.734$. % Dev is the deviation from the expected charge.

tions in this composition range as can be seen below in Fig. 6 (for example, the effective moment obtained for $SmNi_{0.3}Co_{0.7}O_3$ between 200 and 300 K is 1.30 μ_B while the theoretical moment for LS Ni^{3+} and LS Co^{3+} is 0.95 μ_B). We have denoted this region as **SPI** in Fig. 1 in order to differentiate it from other paramagnetic regions where the experimental paramagnetic moment coincides with the expected moment for a mixture of LS Co^{3+} and LS Ni^{3+}. In this work, we have noticed that the different current transport properties and magnetic properties are reflected in the structural parameters of the $SmNi_{1-x}Co_xO_3$ samples. As it can be seen in Fig. 4, none of these parameters follows the Vegard's law. First, there is a small anomaly for $x = 0.03$ and 0.075 in the lattice parameters and unit cell volume. This feature can be related with the MI transition driven by Co doping at room temperature in the current transport properties. However, the most evident characteristic is a positive departure from the Vegard's law in the $0.2 < x < 1$ range for all curves. This second anomaly could be related to changes in the current transport and in the magnetic properties in that composition range.

Figure 5 shows the average d_{M-O}, obtained from Rietveld analysis for $SmNi_{1-x}Co_xO_3$. Figure 3 (Volume vs x) and Fig. 4 (d_{M-O} vs x) exhibit similar features, which suggest again that the main structural effects arise from the M sublattice. The smallest d_{M-O} corresponds to $SmCoO_3$ and agrees with the expected Co–O distance for a LSCo^{3+} (22, 24). The fitted Ni–O distance, d_{Ni-O}, is larger than 1.94 Å, the expected value for a LS Ni^{3+} ion (22, 23), but it agrees with previous neutron diffraction results in $SmNiO_3$ (6, 19). Different d_{Ni-O} values have been determined for each of the $RNiO_3$ at room temperature depending on the current transport character. There is a relationship between d_{Ni-O} and the unit cell expansion shown by these compounds when either the temperature-driven or the composition-driven MI transition appears. As an example, metallic $LaNiO_3$, $PrNiO_3$, and $NdNiO_3$ show at room temperature $d_{Ni-O} < 1.945$ Å, but semiconducting $SmNiO_3$ or $EuNiO_3$ show $d_{Ni-O} > 1.945$ Å (21).

For the sake of clarity, we have plotted in Fig. 5 the expected d_{M-O} for insulating and metallic compounds. In the first case we have interpolated the data obtained for $SmNiO_3$ and for $SmCoO_3$ at room temperature. In the second case the interpolation has been made taking the d_{Ni-O} in the metallic $SmNiO_3$, 1.948 Å at 410 K (6). The replacement of Ni by Co has two noticeable effects on d_{M-O} (both of them are similar to the already described in the volume evolution). For low Co contents there is a sharp

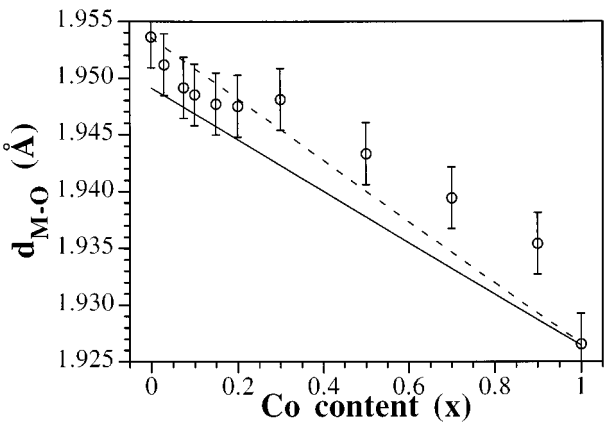

FIG. 5. Average bond lengths between transition metal and oxygen atoms for the $SmNi_{1-x}Co_xO_3$ series. The broken line is the expected bond length when the ionic radius of low-spin Ni^{3+} in metallic samples is considered. The dotted line is the expected bond length considering the ionic radius of low-spin Ni^{3+} in insulating samples.

decrease in d_{M-O}. It is related to the increase of the conductivity in the samples. We suppose that is a signature of the MI transition driven by cobalt doping. Therefore, as Ni is replaced by Co, d_{M-O} decreases and takes the expected values for metallic samples at room temperature ($0.075 \leq x \leq 0.2$). This change can also be noticed in the MO_6 octahedra for $x \leq 0.10$. The NiO_6 octahedra are not completely regular in $SmNiO_3$ at room temperature (LS Ni^{3+} can be Jahn–Teller ions). The values of d_{Ni-O} range from 1.977 to 1.941 Å. This distortion decreases with Co doping and d_{M-O} ranges from 1.955 to 1. 942 Å for the metallic $x = 0.1$.

The second singular feature is observed for $0.3 \leq x \leq 0.9$. In this range, d_{M-O} show values larger than the expected values, see Fig. 5. This behavior cannot be explained just by a Ni–O insulating bond and it points to a different electronic state in the M sublattice. It is well known that Co electronic state changes with increasing temperature (9, 10). In order to study it, we have carried out magnetic measurements from 5 up to 700 K on a selected set of samples. The results obtained for $SmNiO_3$, $SmCoO_3$, and $SmNi_{0.3}Co_{0.7}O_3$ are shown in Fig. 6. We have also plotted the curve obtained for $SmScO_3$ as a reference to account for the magnetic behavior of Sm^{3+} ions. In order to see the magnetic behavior of the different samples more clearly, we have subtracted the magnetic signal of $SmScO_3$ from the signal of the other compounds. The results are shown in the inset of Fig. 6. $SmNiO_3$ shows a magnetic anomaly at 220 K that corresponds to the magnetic ordering of the Ni^{3+} ions (4, 6). The $SmCoO_3$ and $SmScO_3$ curves are very similar below room temperature and, consequently, the subtracted curve (see inset) is practically zero. This indicates a common paramagnetic contribution due to Sm^{3+} ions and, therefore, cobalt ions in $SmCoO_3$ are of low spin in this temperature range ($\mathbf{S} = 0$ for Sc^{3+} and LS Co^{3+}). Above room temperature, a spin transition is developed by Co^{3+} ions in $SmCoO_3$ and the paramagnetic signal increases with increasing the temperature. The kind of Co^{3+} spin state at high temperatures, either HS or IS, is currently an open question (9, 10). $SmNi_{0.3}Co_{0.7}O_3$ shows a similar magnetic anomaly to $SmCoO_3$ at the same temperature. It is plausible to relate this anomaly to the same kind of spin transition in the Co^{3+} ions. However, the magnetic behavior below room temperature is completely different to $SmCoO_3$. The high paramagnetic signal shown by $SmNi_{0.3}Co_{0.7}O_3$ below 300 K cannot be accounted for considering only LS Ni^{3+} and LS Co^{3+} ions. Different electronic states for these ions must be present in this sample at high temperatures and they are responsible for the ferromagnetic interactions shown by this sample at low temperatures (3). Analogous results have been obtained for $SmNi_{1-x}Co_xO_3$ samples with $0.3 \leq x < 0.9$. We think that these new electronic configurations (Ni^{2+}, IS or HS Co^{3+}) are reflected in the d_{M-O} of $SmNi_{1-x}Co_xO_3$ samples but they are likely a minority in the M sublattice. The last statement is supported by both the spin transition from LS Co^{3+} to higher spin states observed in $SmNi_{0.3}Co_{0.7}O_3$, and the bond valence calculations in agreement with a majority of LS Ni^{3+} and LS Co^{3+} in these samples. In short, it seems to be a correlation between the values obtained for d_{M-O}, 0.005 Å larger than the expected by the Vegard's law and different electronic configurations from Ni^{3+} and Co^{3+} in low-spin states.

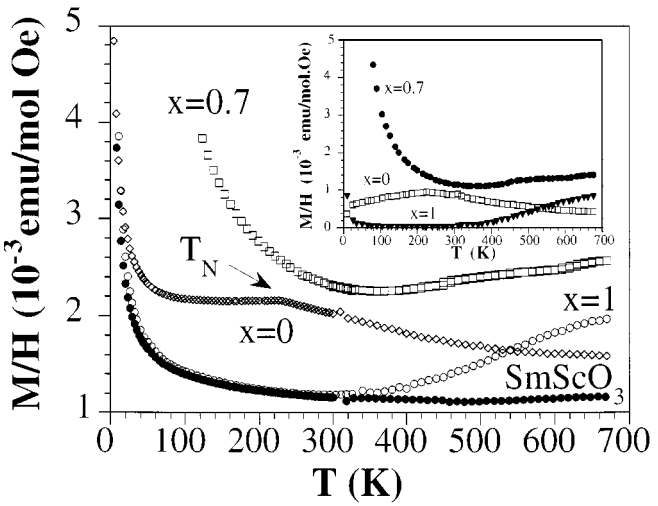

FIG. 6. M/H vs temperature ($\mu_0 H = 0.1$ T) for $SmScO_3$, $SmNiO_3$, $SmCoO_3$, and $SmNi_{0.3}Co_{0.7}O_3$.

The importance of the MO_6 octahedra tilts in the distortion of RMO_3 oxides with perovskite structure has already been described (17). The $\langle M\text{–O–}M \rangle$ bond angle is a measurement of the value of these tilts (20). Moreover, in RMO_3 perovskite the conduction bandwidth of $3d$ parentage is proportional to $\cos[180^\circ - \langle M\text{–O–}M \rangle]$. So, the larger the $\langle M\text{–O–}M \rangle$ angle, the wider the conduction bandwidth (4, 11, 13). Thus, conductivity behaviors are mainly brought about by the e_g bandwidth, the number of carriers, and different localization effects (electron–electron correlation, structural disorder). In a simple electron gas approximation, $SmNi_{1-x}Co_xO_3$ are systems with a full t_{2g} band and a partially filled e_g band, in which the number of carriers varies from $\frac{1}{4}$ ($SmNiO_3$) to 0 ($SmCoO_3$). Figure 7 shows how the $\langle M\text{–O–}M \rangle$ angle increases slightly as the Co content increases. This change is not continuous. $\langle M\text{–O–}M \rangle$ changes at the ends of the series but it remains practically unchanged for intermediate compounds. The sudden increase in $\langle M\text{–O–}M \rangle$ for $x \leq 0.1$ is likely a new feature of the change in the transport properties, i.e., the MI transition. Further substitution of Ni by Co does not change this angle significantly, but compounds with $x > 0.3$ are semiconductors. This fact suggests that disorder effects, and not a bandwidth change, are the origin of the thermally activation conduction for $x \geq 0.3$. The effect of the cation

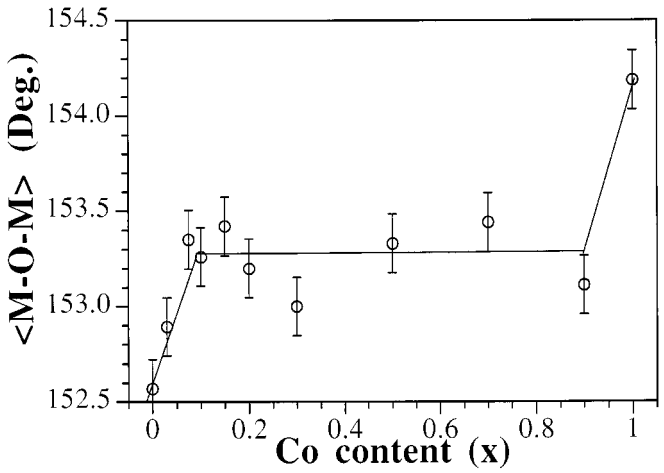

FIG. 7. Average bond angle between adjacent MO_6 octahedra vs cobalt concentration along the $SmNi_{1-x}Co_xO_3$ series.

disorder, i.e., an Anderson transition, is thought to be the cause of the semiconducting properties for $x \geq 0.3$ (3). Finally, $SmCoO_3$ shows the largest $\langle M\text{–O–}M \rangle$ bond angle with no cation disorder. However, $SmCoO_3$ is a semiconductor with an activation energy of 0.2 eV (11). $SmCoO_3$ semiconducting properties are due to the electronic LS Co^{3+} configuration ($t_{2g}^6 e_g^0$), without electrons in the conduction band of e_g-parentage.

In order to complete the structural study we have also studied the environment of the Sm^{3+} ion. The variations of the eight nonequivalent Sm–O distances are shown in Fig. 8. Sm–O environment is a strongly distorted dodecahedron. Considering a 3-Å cutoff, Sm^{3+} can be considered 8 coordinated instead of 12 coordinated as in cubic perovskites. The average nearest-neighbour Sm–O bond lengths decreases with increasing Co content in agreement with a lower unit cell for $SmCoO_3$.

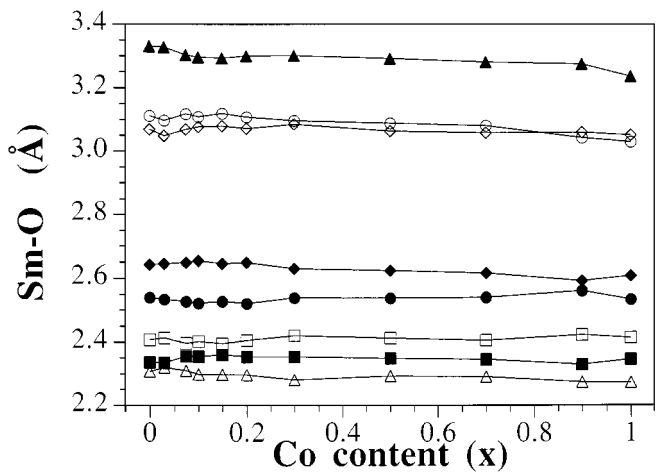

FIG. 8. Variation of the Sm–O bond lengths vs cobalt concentration for the Sm–O polyhedron in $SmNi_{1-x}Co_xO_3$ samples.

4. CONCLUSION

The structure of the $SmNi_{1-x}Co_xO_3$ series has been extensively studied by means of X-ray diffraction at room temperature. Our results point out a relationship between small structural changes and the variations of the macroscopic properties. Variations of d_{M-O}, $\langle M\text{–O–}M \rangle$ angles have been described when Co doping drives a MI transition ($x \leq 0.1$). The main feature is observed along the series, it concerns the bond lengths between M and oxygen atoms. Metallic samples show the smallest bond lengths while the largest bond lengths correspond to the samples that show large magnetoresistance and spin-glass behavior at low temperatures. This feature could be related with an effective charge transfer between Ni^{3+} and Co^{3+} ions. The electronic state for these ions is different from that expected for LS Ni^{3+} and LS Co^{3+}. A magnetic property has been reflected (see Fig. 5) in the crystallographic parameters. In this way, the search of anomalies in the bond lengths in different oxides could be an indication of such a kind of charge transfer among M ions.

ACKNOWLEDGMENTS

This work has been supported by the CICYT Project No. MAT96-0491. One of us (J.P.) acknowledges his doctoral and postdoctoral fellowships to the M.E.C. (Spain).

REFERENCES

1. N. Mott, "Metal–Insulator Transitions." Taylor & Francis, London, 1990.
2. P. A. Cox, "Transition Metal Oxides. An Introduction to Their Electronic Structure and Properties." Clarendon Press, Oxford, 1995.
3. J. Pérez-Cacho, J. Blasco, J. García, and J. Stankiewicz, *Phys. Rev. B* **59,** 14424 (1999).
4. P. Lacorre, J. B. Torrance, J. Pannetier, A. I. Nazzal, P. W. Wang, and T. C. Huang, *J. Solid State Chem.* **91,** 225 (1991); J. B. Torrance, P. Lacorre, A. I. Nazzal, E. J. Ansaldo, and Ch. Niedermayer, *Phys. Rev. B* **45,** R8209 (1992).
5. J. Pérez-Cacho, J. Blasco, J. García, M. Castro, and J. Stankiewicz, *J. Phys. Condens. Matter* **11,** 405 (1999).
6. J. Rodriguez-Carvajal, S. Rosenkranz, M. Medarde, P. Lacorre, M. T. Fernandez-Díez, F. Fauth, and V. Trounov, *Phys. Rev. Lett.* **57,** 456 (1998).
7. J. A. Alonso, J. L. García-Muñoz, M. T. Fernández-Díaz, M. A. G. Aranda, M. J. Martínez-Lope, and M. T. Casais, *Phys. Rev. Lett.* **82,** 3871 (1999).
8. M. L. Medarde, *J. Phys. Condens. Matter* **9,** 1697 (1997).
9. M. A. Señarís-Rodríguez and J. B. Goodenough, *J. Solid State Chem.* **116,** 224, (1995); J. B. Goodenough and P. M. Raccah, *J. Appl. Phys.* **36,** 1031 (1965).
10. S. Yamaguchi, Y. Okimoto, and Y. Tokura, *Phys. Rev. B* **53,** R2926 (1996); S. Yamaguchi, Y Okimoto, and Y. Tokura, *Phys. Rev. B* **55,** R8666 (1997).

11. S. Yamaguchi, Y. Okimoto, and Y. Tokura, *Phys. Rev. B* **54,** R11022 (1996).
12. A. K. Raydchaudhuri, *Adv. Phys.* **44,** 21 (1995).
13. J.Pérez, J. García, J. Blasco, and J. Stankiewicz, *Phys. Rev. Lett.* **80,** 2401 (1998).
14. J. Rodriguez-Carvajal, *Physica B* **192,** 55 (1990).
15. I. D. Brown, *Acta Crystallogr. Sect. B* **48,** 553 (1992); N. E. Brese and M. O'Keeffe, *Acta Crystallogr. Sect. B* **47,** 192 (1991).
16. A. S. Wills and I. D. Brown, "VaList," computer program, 1999. [From willsas@netscape.net]
17. A. M. Glazer, *Acta Crystallogr. Sect. B* **28,** 3384 (1972); A. M. Glazer, *Acta Crystallogr. Sect. A* **31,** 756 (1975).
18. M. Abbate, J. C. Fuggle, A. Fujimori, L. H. Tjeng, C. T. Chen, R. Potze, G. A. Sawatzky, H. Eisaki, and S. Uchida, *Phys. Rev. B* **47,** 16124 (1993); T. Mizokawa, A. Fujimori, T. Arima, Y. Tokura, N. Mori, and J. Akimitsu, *Phys. Rev. B* **52,** 13,865 (1995); J. García, J. Blasco, M. G. Proietti, and M. Benfatto, *Phys. Rev B* **52,** 15,823 (1995).
19. X. Liu and C. T. Prewit, *J. Phys. Chem. Solids* **52,** 441 (1991).
20. J. L. García Muñoz, J. Rodriguez-Carvajal, P. Lacorre, and J. B. Torrance, *Phys. Rev. B.* **46,** 4414 (1992).
21. J. A. Alonso, M. J. Martínez-Lope, and I. Rasines, *J. Solid State Chem.* **120,** 170 (1995); J. A. Alonso, M.J. Martínez-Lope, and M. A. Hidalgo, *J. Solid State Chem.* **116,** 146 (1995).
22. R. D. Shannon, *Acta Crystallogr. Sect. A* **32,** 751 (1976).
23. D. A. Maclean, H. N. Hu, and J. E. Greedan, *J. Solid State Chem.* **30,** 35 (1978).
24. M. Castellanos and A. R. West, *J. Chem. Soc. Faraday Trans.* **76,** 2159 (1980).